Unified model for a nonlinear pulse propagation in composites and optimization of THz generation

A. Husakou*
Max Born Institute, Max-Born-Straße 2a, 12489 Berlin, Germany

O. Fedotova, R. Rusetsky, and O. Khasanov
Scientific-Practical Materials Research Centre of National Academy of Sciences of Belarus, P. Brovki Street 19, 220072 Minsk, Belarus

T. Smirnova and A. Fedotov
Belarus State University, Niezaliežnasci Avenue 4, 220030 Minsk, Belarus

T. Apostolova
Institute for Nuclear Research and Nuclear Energy, Bulgarian Academy of Sciences, Tsarigradsko Chausse 72, 1784 Sofia, Bulgaria and Institute for Advanced Physical Studies, New Bulgarian University, 1618 Sofia, Bulgaria

I. Babushkin
Institute of Quantum Optics, Leibniz University Hannover, Welfengarten 1, 30167 Hannover, Germany; and Cluster of Excellence PhoenixD (Photonics, Optics, and Engineering - Innovation Across Disciplines), 30167 Hannover, Germany; and Max Born Institute, Max-Born-Straße 2a, 12489 Berlin, Germany

U. Sapaev
Tashkent State Technical University, University Street 2, 100097 Tashkent, Uzbekistan

(Received 12 January 2023; accepted 22 June 2023; published 12 July 2023)

We describe a unified numerical model which allows fast and accurate simulation of nonlinear light propagation in nanoparticle composites, including various effects such as group velocity dispersion, second- and third-order nonlinearity, quasi-free-carrier formation and plasma contributions, exciton dynamics, scattering, and so on. A developed software package, Simulator of Light Propagation in Composites (SOLPIC), is made available for the community. Using this model, we analyze and optimize efficient generation of terahertz (THz) radiation by two-color pulses in ZnO–fused-silica composite, predicting an efficiency of 3%. We compare the role of various nonlinear effects contributing to the frequency conversion and show that the optimum conditions of THz generation differ from those expected intuitively.

DOI: 10.1103/PhysRevA.108.013506

I. INTRODUCTION

Terahertz (THz) technology has attracted a lot of attention in recent years, since it provides unique experimental tools and techniques in nonlinear and time-domain spectroscopy, biology and medicine, remote sensing, security screening, and information and communication systems (see, e.g., Refs. [1–4]). For generation of THz radiation, different techniques were proposed, such as two-color ionizing femtosecond pulses in gases [5–10] and surface plasmas [11], as well as optical rectification of intense ultrashort pulses in nonlinear crystals [12–16], which provide a basis for compact low-intensity devices. The needs of the THz technology require, however, extension of the range of the available techniques and materials, in order to provide a flexible design required in multifarious applications. Following this line, investigations of THz generation in various media such as water [17], strongly magnetized plasma [18], and centrosymmetric two-photon resonant molecular impurities [19] were performed. Emission of terahertz radiation with broad bandwidth by femtosecond photoexcitation of spintronic materials (ferromagnetic and synthetic multiferroic heterostructures) was also reported recently [20,21].

Nanoparticle (NP) composites were actively investigated in the past as a nonlinear material (e.g., Refs. [22–24]), and their particular strength lies in the flexibility of their design leading to unusual properties such as, e.g., a negative refractive index [25]. However, surprisingly, to our knowledge they have not attracted attention as a medium for THz generation. In this paper, we close this gap by conceptualizing a numerical model suitable for simulation of THz generation in nanocomposites. A range of linear and nonlinear effects such as group velocity dispersion, second- and third-order nonlinearity, quasi-free-carrier formation, exciton dynamics, and so on are encompassed by the developed model. We use it to explore THz generation by two-color pulses in nanoparticle composites, to elucidate the contributions of different

*gusakov@mbi-berlin.de

frequency conversion mechanisms, and to predict efficiencies in the few-percent range.

The applicability of the above model is, in fact, much broader than mere simulation of THz generation; a wide range of nonlinear effects such as soliton dynamics and supercontinuum generation, frequency conversion, multilevel dynamics and electromagnetically induced transparency, and so on can be studied using this unified approach. With this in mind, we have created extensive documentation of the Simulator of Light Propagation in Composites (SOLPIC) code, and made the code publicly available [26], in the hope that it will be useful to the optical community for investigations of the nonlinear processes in nanocomposites and other materials.

The paper is organized as follows. In Sec. II, we present the numerical model, including the detailed formalism for all the relevant mechanisms. In Sec. III, we optimize the THz generation by two-color pulses and analyze the role of different parameters. A summary of the paper is given in the Conclusion.

II. THEORETICAL MODEL

We consider a composite consisting of two components, a homogeneous host material and spherical NPs (inclusions) randomly distributed in space. We assume a sufficiently low (typically a few percent or below) filling fraction of the inclusions so that neither percolation nor interaction between the inclusions plays a role. We consider homogeneous inclusions to be sufficiently small with diameter below the light wavelength so that effective-medium theory can be applied. Note that we do not place any limitations on the nature of host and inclusion materials, i.e., either of them could be a dielectric, a metal, or a semiconductor. We do not require point symmetry in the host material or in the inclusions, so that the second-order susceptibility can be nonzero in either material. The model is designed to simulate light propagation over relatively short distances of a few millimeters, below the damage threshold, and without back reflection; therefore a (1+1)-dimensional [(1+1)D] treatment using the unidirectional propagation equation [27] is the most suitable. We note that in the case of THz propagation, a straightforward extension of this treatment to (2+1)D can be required even for relatively broad pump beams with beamwidth around 30 μm.

Under these conditions, the following effects have to be taken into account: linear dispersion including intrinsic and scattering losses, second- and third-order optical nonlinearities, photoionization accompanied by ionization losses, and plasma dynamics. In addition, transitions between excitonic states can play a significant role in the inclusion response, in particular for the generation of new frequencies in the THz range. Among the effects which were neglected in this treatment are thermal effects (due to the slow, nanosecond-scale response), coupling to phonons (because of the relatively slow, picosecond-scale response), Raman scattering (which is typically weaker than instantaneous nonlinearities), anisotropy of the host material (due to the manufacturing limitations for composites), deviations of the inclusion from a sphere (because of typical manufacturing conditions), and generation of high-order harmonics (because of the considered intensity ranges).

The following unidirectional propagation equation is used to model the light propagation in a homogeneous medium [27,28]:

$$\frac{\partial E(z,\omega)}{\partial z} = -i\left(\frac{[\sqrt{\epsilon(\omega)}-n_g]\omega}{c} - \beta(\omega_0)\right)E(z,\omega) - \frac{i\omega}{2c\sqrt{\epsilon(\omega)}}P_{\mathrm{NL}}(z,\omega), \tag{1}$$

where $E(z,\omega)=\hat{F}E(z,t)=\int_{-\infty}^{\infty}E(z,t)\exp(-i\omega t)dt$ is the Fourier transform $\hat{F}$ of the electric field $E(z,t)$, z is the propagation coordinate, $\epsilon(\omega)$ is the linear dielectric permittivity (generally speaking, complex-valued to include loss mechanisms), n_g is the group refractive index, ω_0 is a characteristic frequency of the pulse spectrum, $\beta(\omega)=\sqrt{\epsilon(\omega)}\omega/c$, and $P_{\mathrm{NL}}(z,\omega)$ is the Fourier transform of the nonlinear part of the polarization. We would like to emphasize that no slowly varying envelope approximation was used and $E(z,t)$ represents the real-valued field including the carrier oscillations. This approach yields a unified treatment for a pulse with arbitrary spectral content, which is particularly important for extremely broad spectra.

A. Linear dispersion

The effective-medium theory allows us to substitute a homogenized medium with appropriately defined effective material parameters for the composite material. The effective refractive index of a composite can be expressed as [28]

$$n_{\mathrm{eff}} = \left[(1-f)\epsilon_h + f\epsilon_i\frac{3\epsilon_h}{2\epsilon_h+\epsilon_i} + 2i\left(\frac{\epsilon_h-\epsilon_i}{2\epsilon_h+\epsilon_i}\right)^2\left(\frac{r_{\mathrm{NP}}\omega\sqrt{\epsilon_h}}{c}\right)^3\right]^{1/2}, \tag{2}$$

where f is the volume filling factor of the inclusions, r_{NP} is their radius, and ϵ_h and ϵ_i are the frequency-dependent dielectric functions of the host and of the inclusions, correspondingly. The last term in the square brackets describes scattering losses.

B. Second- and third-order nonlinearities

The second- and third-order nonlinear processes can also be described in the framework of the effective-medium theory. The expression for the effective second-order susceptibility looks like [29]

$$\chi^{(2)}_{\mathrm{eff}}(\omega_1=\omega_2+\omega_3;\omega_2,\omega_3) = (1-f)\chi^{(2)}_h + fx(\omega_1)x(\omega_2)x(\omega_3)\chi^{(2)}_i, \tag{3}$$

where $\chi^{(2)}_h$ and $\chi^{(2)}_i$ are the susceptibilities of host and inclusion materials, correspondingly. Note that we neglected the frequency dependence of the susceptibilities of host and inclusions, which is a good assumption far from resonances. The quantity $x(\omega)$ is the ratio of the local field inside the inclusion and the incident field:

$$x(\omega) = \frac{3\epsilon_h(\omega)}{2\epsilon_h(\omega)+\epsilon_i(\omega)}. \tag{4}$$

Here, we note that due to photoionization as described below, the $\epsilon_i(\omega)$ and therefore x, strictly speaking, depend on time due to buildup of plasma during the pulse. However, in the current simulation we neglect this dependence, assuming that the corresponding change in $\epsilon_i(\omega)$ is small and that we are far from the plasmonic resonance given by $2\epsilon_h(\omega) = -\epsilon_i(\omega)$.

Similarly, for the effective third-order susceptibility we write [29]

$$\chi^{(3)}_{\text{eff}}(\omega_1 = \omega_2 + \omega_3 + \omega_4; \omega_2, \omega_3, \omega_4) = (1-f)\chi^{(3)}_h + f x(\omega_1)x(\omega_2)x(\omega_3)x(\omega_4)\chi^{(3)}_i, \quad (5)$$

where $\chi^{(3)}_h$ and $\chi^{(3)}_i$ are the susceptibilities of the host and inclusion materials, correspondingly. The final expressions which were used to calculate the corresponding polarizations look like

$$P_{\chi^{(2)}}(z,\omega) = (1-f)\epsilon_0\chi^{(2)}_h\hat{F}E(z,t)^2 + f\epsilon_0\chi^{(2)}_i\hat{F}[\hat{F}^{-1}\{E(z,\omega)x(\omega)\}^2], \quad (6)$$

$$P_{\chi^{(3)}}(z,\omega) = (1-f)\epsilon_0\chi^{(3)}_h\hat{F}E(z,t)^3 + f\epsilon_0\chi^{(3)}_i\hat{F}[\hat{F}^{-1}\{E(z,\omega)x(\omega)\}^3]. \quad (7)$$

C. Plasma dynamics

Let us turn to the description of plasma formation and dynamics. In the framework of SOLPIC, we consider a case when the ionization potential I_p of the inclusions is lower than that of the host material, so that due to the sensitive dependence of the polarization rate on the ionization potential we can neglect plasma formation in the host material.

The contribution from the plasma is determined by the average displacement $\langle d\rangle(z,t)$ of the electron from the equilibrium position in the parent "molecule," whereby by a "molecule" we denote an atom or a group of atoms of the solid-state material which can provide a single ionization event. Furthermore, it is determined by the relative ionization of the solid state $\rho(z,t)$, which is the ratio of the conduction-band electron density to the density of "molecules":

$$P_{\text{plasma}}(z,\omega) = -N_{\text{mol}}e\hat{F}[\langle d\rangle(z,t)\rho(z,t)]. \quad (8)$$

Here, N_{mol} is the concentration of the molecules, and $e = 1.6\times10^{-19}$ is the electron charge. The above expression would be valid in a homogeneous medium; however, as it refers to a polarization which occurs inside of NPs, in contrast to averaged macroscopic polarization, in the case of effective-medium theory it has to be additionally multiplied by $x(\omega)$. For the origin of this factor and further details, see Ref. [29].

The dynamics of the quantity $\langle d\rangle(z,t)\rho(z,t)$ is given by [30]

$$\frac{\partial(\langle d\rangle(z,t)\rho(z,t))}{\partial t} = \langle v\rangle(z,t) + x_0\Gamma(t), \quad (9)$$

where $\langle v\rangle$ is the average velocity of electrons and $x_0 \simeq -I_p/eE(t)$ is the initial displacement of the electron immediately after the ionization event, I_p being the band gap. It can be shown that the second term describes the energy loss of the pulse due to the photoionization. The dynamics of $\langle v\rangle(z,t)\rho(z,t)$ is given by Newton's second law as

$$\frac{\partial(\langle v\rangle(z,t)\rho(z,t))}{\partial t} = -\frac{eE(z,t)}{m_e}\rho, \quad (10)$$

where m_e is the effective electron mass near the bottom of the conduction band. Here, we neglect the initial displacement and velocity of the electron just after the ionization.

The dynamics of the relative plasma density ρ is given by

$$\frac{\partial\rho}{\partial t} = \Gamma(\hat{F}^{-1}[x(\omega)E(z,\omega)]), \quad (11)$$

where $x(\omega)E(z,\omega)$ is the local field inside of inclusions, which determines the photoionization rate Γ.

D. Ionization rate

Depending on the relation between the frequency of pump light and the ionization potential of inclusions, we consider two models for the ionization rate. For the case when the energy of pump photons is much smaller than the ionization potential, the photoionization occurs either in a multiphoton regime or in a tunneling regime, as determined by the intensity and the Keldysh parameter. Here we utilize so-called Yudin-Ivanov model [31], which provides a formalism for both of these regimes in a unified way. This model was initially developed for isolated atoms; its use for solid states is justified in the case of a negligible anharmonicity of the bands in the center of the Brillouin zone.

The cycle-resolved ionization rate Γ is given (in atomic units, that is, with frequency ω, time t, and field $\mathcal{E}$ measured in the corresponding Hartree units $\omega_a = 0.26$ rad/as, $t_a = 24.2$ as, $x_a = 0.0529$ nm, and $\mathcal{E}_a = 514.2$ V/nm) by

$$\Gamma(z,t) = \frac{\pi}{\tau_T}\exp\left(-\sigma_0\frac{\langle 2\mathcal{E}(z,t)^2\rangle}{\omega^3}\right)\left[\frac{2\kappa^3}{\sqrt{\langle 2\mathcal{E}(z,t)^2\rangle}}\right]^{2Z/\kappa} \times \exp\left[-\frac{\mathcal{E}(z,t)^2}{2\omega^3}\sigma_1\right]. \quad (12)$$

Here, $\tau_T = \kappa/E(z,t)$, $\kappa = \sqrt{I_p/(\hbar\omega_a)}$, $\sigma_0 = \frac{1}{2}(\gamma^2 + \frac{1}{2})\ln C - \frac{1}{2}\gamma\sqrt{1+\gamma^2}$, $\gamma = \omega\tau_T$, Z is the effective atomic charge, $C = 1 + 2\gamma\sqrt{1+\gamma^2} + 2\gamma^2$, and $\sigma_1 = \ln C - 2\gamma/\sqrt{1+\gamma^2}$. The quantity $\langle E(z,t)^2\rangle$ is the averaged value of the squared electric field over the past few periods (5 fs is assumed in this paper).

The Yudin-Ivanov model was initially derived for gases; its applicability for solid states, while generally justified for materials with tight binding, is not strictly established. We have benchmarked the Yudin-Ivanov model by comparing it with the numerical solution of the time-dependent Schrödinger equation in the single-active-electron approximation [32]. In this approach the empirical pseudopotential method was used for describing the electron band structure of ZnO [33]. We have found that the difference in the ionization rates does not typically exceed one order of magnitude. This difference is, in fact, not very significant: Because of the thresholdlike behavior of the ionization rate, it leads to only a slight shift in the intensity at which strong plasma generation is reached.

For the special case where the energy of pump photons is around two ionization potentials, it is preferable to use

the two-photon formalism [34] and write the cycle-resolved ionization rate Γ [in *Système International* (SI) units] as

$$\Gamma(z,t) = \frac{2e^4 x_a^4 \nu}{\hbar^4 \omega_0^2 [(2\omega_0 - I_p/\hbar)^2 + \nu^2]} \langle E(z,t)^2 \rangle E(z,t)^2, \tag{13}$$

where ν is the relaxation constant of the two-photon transition.

We also note that for situations where a significant portion of the pump spectrum lies beyond the band gap, it might be necessary to include one-photon absorption. This is not the case in the current pump consideration.

E. Contribution by excitons

Finally, we include the nonlinear polarization due to excitons in the treatment. We consider multiple excitonic levels and utilize the standard Bloch equations for the description of the ionization. The dynamics of the density matrix ρ_e is given by (see, e.g., Ref. [34])

$$i\hbar \frac{\partial \rho_e}{\partial t} = [H, \rho_e], \tag{14}$$

where $H = H_0 + H_{\text{int}}$. Here, H_0 is the Hamiltonian of the system in the absence of excitation given by the diagonal elements corresponding to the exciton energies, and H_{int} is the interaction Hamiltonian, whose components $H_{\text{int},ij}$ are related with the corresponding dipole transition moments of excitons eM_{ij}:

$$H_{\text{int},ij} = eM_{ij}\hat{F}^{-1}[E(z,\omega)x(\omega)]. \tag{15}$$

In addition, polarization decay (decay of the off-diagonal elements of ρ_e) with decay time T_2 and decay of the population to the ground state with decay time T_1 are included. In order to avoid numerical instabilities, the normalization of the density matrix ρ is performed every few steps in time, by (a) enforcing $0 \leqslant \rho_{e,ii} \leqslant 1$, (b) enforcing $\text{Tr}(\rho_e) = 1$, and (c) adjusting the nondiagonal elements which exceed the maximum possible value determined by the corresponding level populations.

The excitonic polarization is then defined in a standard way as

$$P_{\text{exc}}(z,\omega) = x(\omega)\hat{F}[f\text{Tr}(\rho_e M)]. \tag{16}$$

We solve the propagation equation using an extended split-step method, whereby each of the contributions to the polarization is treated subsequently, which allows us to reduce the accumulation of numerical error. Nonlinear steps are performed using the Runge-Kutta approach, the order of which can be selected between 1, 2, and 4. A fixed step of the grid both in time and in the propagation coordinate is used. The appearance of numerical artifacts during the propagation is monitored by tracing the total pulse energy as well as the total energy absorbed at the boundaries of the numerical time window.

F. Benchmarking of the model

In order to establish the reliability and accuracy of the developed model and the numerical code, we have performed benchmarking against the available experimental and numerical data. A large number of investigations have been devoted to THz generation in gaseous systems, as contrasted with the limited results available for composites. Therefore we have chosen to benchmark our code against one of the cases of THz generation in a noble gas related to plasma generation [35]. In agreement with the parameters given in Ref. [35], we have considered two-color excitation with 30-fs pulses at 815 and 407 nm with peak intensities of 100 and 20 TW/cm^2, correspondingly, with no temporal delay between the pulses. Propagation over the focal region of 1 cm through argon at a pressure of 0.79 atm, in accordance with the setup of Ref. [35], was simulated. We predict a THz generation efficiency of 0.85×10^{-4}, which is in reasonable agreement with the experimental efficiency of 0.54×10^{-4}, given the uncertainty inherent to photoionization processes [36]. In addition, we have compared the widths of the THz spectra. Our simulations predict a 108 THz width, while in Ref. [35] a 75 THz spectral width was observed, with quite satisfactory agreement given that the experimental spectral width was reduced by absorption in the elements of the detection apparatus.

III. NUMERICAL RESULTS AND DISCUSSION

In order to exemplify the above model and the functioning of SOLPIC, we present in this section a simulation of THz generation. We consider a composite of ZnO inclusions in an amorphous SiO_2 matrix. Phenomenological Sellmeier-type expressions were used to describe dispersion on ZnO [37] and SiO_2 [38]. Absorption of photons with energies above the corresponding band gaps was directly included; however, absorption at the phonon band was disregarded since it provides losses in a few narrow bands, which will not significantly influence the generated THz radiation as a whole. Similarly, experimental data on second-order [39] and third-order [40,41] susceptibility of bulk ZnO and third-order susceptibility of SiO_2 [42] were used. We estimated the value of T_2 as 50 fs from Ref. [43] and used $T_1 = 2T_2$. For ZnO, the typical exciton size is larger than interatomic distance, meaning that we are dealing with Wannier-Mott-type excitons. In the case of sufficiently small inclusions, the exciton is bounded by the inclusion boundaries; therefore its wave functions (as well as energy levels and dipole momenta) are better described, instead of by a hydrogenlike potential, by a constant potential inside a sphere [44] with a step on its boundary. We have taken into account the five lowest excitonic levels, with the field-free Hamiltonian H_0 being given by the excitonic levels provided by Eq. (10) of Ref. [45]. Typical values of the off-diagonal dipole momenta, as calculated by this approach, are $H_{\text{int},ii} = 3 \times 10^{-28}$ C m, for the same-size NPs with a radius of 2.5 nm which are considered here and hereinafter. For the permanent dipole momenta of ZnO, we have adopted a typical value of $H_{\text{int},ij,i\neq j} = 6.66 \times 10^{-30}$ C m per ZnO molecule, which was used to define the on-diagonal elements of the dipole matrix. We used an ionization potential of 3.37 eV equal to the band gap of ZnO to characterize the transition from valence band to conduction band, and all the presented numerical results correspond to the conditions below the damage threshold of ZnO [46].

The evolution of the field profile and spectra with propagation is illustrated in Fig. 1, for two-color pulsed excitation with pump pulses around 800 and 400 nm, for the conditions given in the caption. In Fig. 1(a), one can see that initial stages

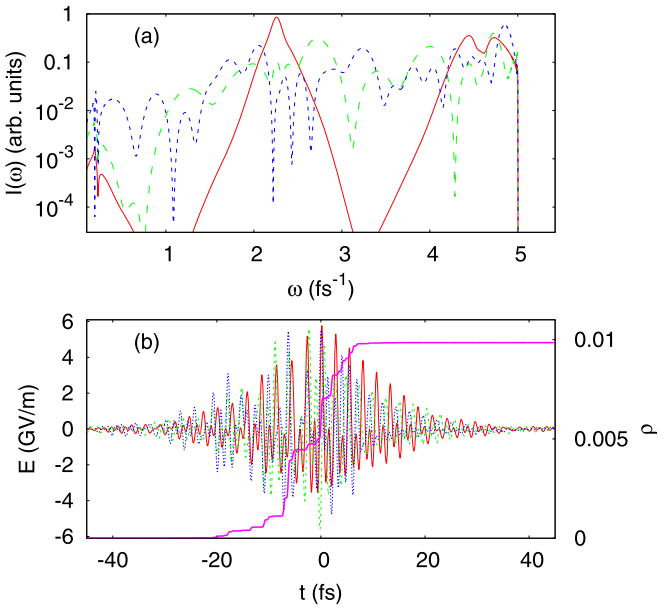

FIG. 1. Dependence of the spectra (a) and the electric field (b) on the propagation length. Fifteen-femtosecond pulses at 2.26 and 4.58 fs^{-1} are considered, with an intensity of 1 TW/cm^2 and propagation lengths of 0.75 μm (red solid curves), 2.25 μm (green long-dashed curves), and 6.75 μm (blue short-dashed curves). In (b), the relative plasma density (thick magenta curve) is additionally shown for a propagation length of 6.75 μm. A composite of ZnO inclusions with $f = 0.03$ in fused silica is considered.

of the propagation are characterized by self-phase-modulation (SPM) with typical spectral sidelobes. At later stages, the spectrum becomes irregular and transforms into a supercontinuum extending up to the absorption edge given by the band gap. The evolution of the temporal profile, shown in Fig. 1(b), shows a gradual reduction in the energy of the electric field, as well as a significantly irregular envelope for longer propagation. This reduction in the maximum field determines the saturation of the THz generation efficiency and is caused both by strong group velocity dispersion for a broad spectrum and by energy absorption due to transition to the conduction band. One can see from the thick magenta curve in Fig. 1(b) that the relative plasma density reaches values of roughly 0.01 after the pulse, which is sufficient to induce significant energy absorption.

In Fig. 2 the evolution of the spectrum in the THz range is shown. One can see that while the THz energy increases at early stages of propagation, for larger propagation lengths the spectrum saturates. Losses around 15 THz and below can also contribute to saturation of generation. After 45 μm propagation length, the efficiency of the generation reaches 3.05%, which is sufficiently high for practical applications.

In order to determine the optimum conditions of THz generation, in Fig. 3 we plot the dependence of the generation efficiency on the distribution of energy between the 830-nm pulse and the 412-nm pulse [Fig. 3(a)], the intensity of pulses [Fig. 3(b)], and the wavelength of the short-wavelength pulse [Fig. 3(c)]. One can see that the efficiency of THz generation is nonzero but very small for the cases where only one of the pulses is present (energy

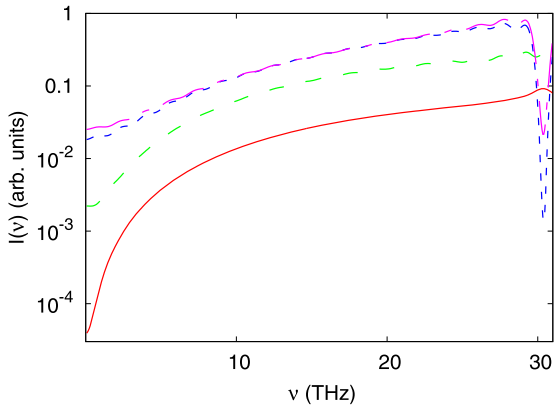

FIG. 2. Dependence of the spectra in the THz range on the propagation distance. We consider 1-TW/cm^2, 15-fs pump pulses at 2.26 and 4.58 fs^{-1}, in a composite of ZnO NPs with filling fraction of $f = 0.03$ in a fused-silica matrix, after a propagation length of 5 μm (red solid curve), 15 μm (green long-dashed curve), 45 μm (blue short-dashed curve), or 50 μm (magenta long-and-short-dashed curve).

fraction of 0 or 1). This indicates that the optical rectification based on the second-order susceptibility of ZnO cannot efficiently generate THz for the considered conditions and that the dominant contribution comes from the third-order susceptibility of ZnO NPs, the third-order susceptibility of SiO_2 being comparatively weak. In an ideal case without pump pulse modification, the efficiency of the THz generation is proportional to $E_{830}^2(E_{\rm tot} - E_{830})$, where E_{830} is the energy of the pulse at 830 nm and $E_{\rm tot} = E_{830} + E_{412}$ is the total energy of the pulses. The maximum efficiency is then reached

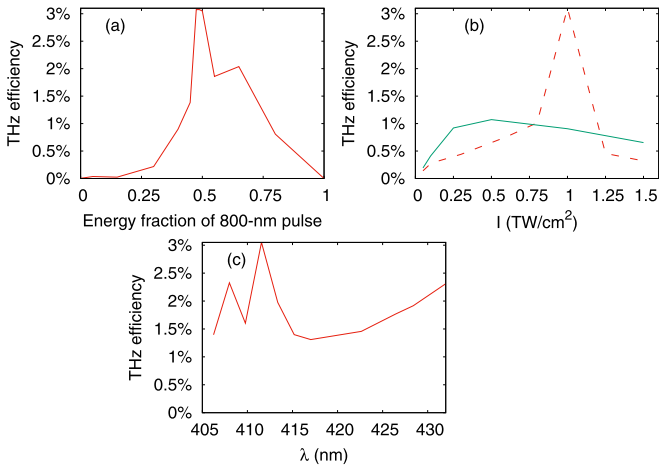

FIG. 3. Dependence of the THz generation efficiency on the energy fraction of the 800-nm pulse (a), the intensity of each of the pump pulses (b), and the wavelength of the second-harmonic pulse (c). A composite of ZnO NPs with $f = 0.03$ in fused silica is considered. In (a), 15-fs pulses at 2.26 and 4.58 fs^{-1} are considered, with a total intensity of 2 TW/cm^2 and propagation length of 50 μm. In (b) we consider 15-fs (red dashed curve) and 150-fs (green solid curve) pulses at 2.26 and 4.58 fs^{-1}. In (c), 1 TW/cm^2, 15-fs pulses are considered, with an IR pulse frequency of 2.26 fs^{-1} and propagation length of 50 μm.

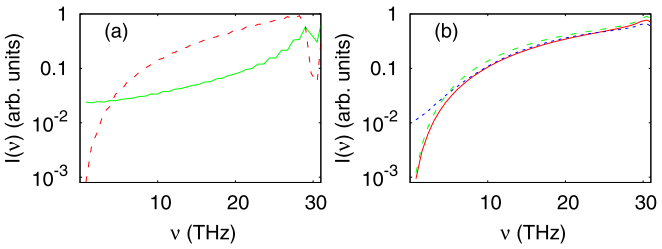

FIG. 4. Spectra in the THz range with (a) the plasma contribution on (green solid curve) and off (red dashed curve) and (b) the exciton contribution on (red solid curve) and off (green long-dashed curve), as well including both the exciton contribution and the permanent dipole moment (blue short-dashed curve). We consider 1-TW/cm^2, 15-fs pump pulses at 2.26 and 4.58 fs^{-1}, in a composite of ZnO inclusions with filling fraction of $f = 0.03$ in a fused-silica matrix, after propagation lengths of 10 μm (a) and 0.75 μm (b).

at $E_{830}/E_{\rm tot} = 1/3$; however, as shown in Fig. 3(a), maximum numerical efficiency is achieved for $E_{830}/E_{\rm tot} = 0.5$. This could be due to strong SPM-induced spectral spreading of high-frequency pulses during the propagation, which needs to be compensated by a relatively higher value of E_{412}. The predicted optimum is in perfect agreement with the results of Ref. [47], where for gases and for relatively low intensity the maximum THz generation efficiency is also achieved at $E_{830}/E_{\rm tot} = 0.5$ ($a_2/a_0 = 1$ in terms of Ref. [47]). In Fig. 3(b), the dependence of the efficiency on the pulse intensity is shown, exhibiting saturation and a decrease after a certain intensity as well as lower efficiencies for longer pulses. We attribute these features to a detrimental contribution of the accumulated plasma, which grows with intensity and pulse duration [cf. Fig. 4(a)]. In Fig. 3(c), the dependence of the efficiency on the wavelength of the short-wavelength pulse exhibits several maxima. Note that while one might expect optimum THz generation for 415 nm, which would correspond to generation of frequencies near zero, our simulations in fact predict a minimum around this value, determined most probably by phase mismatch and losses below 15 THz. We note that in agreement with our results, a similar multiple-peak dependence of the efficiency on frequency was observed also in the context of gas targets [48].

Finally, in order to access the role of plasma and excitons in the THz generation in composites, in Fig. 4 we compare the spectra for a plasma contribution [Fig. 4(a)] and an exciton contribution [Fig. 4(b)] that are switched on and off. One can see that the plasma contribution is significant, both due to the contribution to the refractive index and due to losses, and the absence of a plasma contribution leads to a notable (more than twofold) increase in the efficiency. On the other hand, from Fig. 4(b) one can see that exciton polarization does not provide a strong contribution to the efficiency for the considered parameters. Also, additionally including the permanent dipole momenta, described in the model above, does not significantly increase the efficiency of THz generation, as indicated by the blue short-dashed curve in Fig. 4(b), which is close to the red solid and green long-dashed curves. We note, however, that this conclusion is of limited generality; for other parameters of the medium, excitons can provide the key mechanism of THz generation (see, e.g., Refs. [49,50] and references therein).

IV. CONCLUSION

In this paper we have established a comprehensive numerical model for the simulation of light propagation in composites, including all the relevant physical effects for a broad range of parameters, such as linear dispersion of the composite, second- and third-order nonlinear effects, the plasma contribution, the exciton contribution, and so on. The model was applied to simulate the generation of THz radiation in a ZnO-SiO_2 composite. We have performed optimization of the frequency conversion process, predicting an efficiency of 3.05%. We show that the simulations provide insights into the optimization, such as the power distribution between the pump pulses, which would not be accessible intuitively. We hope that the numerical model and the corresponding software solution will contribute to the capacity of simulations in the area of nonlinear optics.

ACKNOWLEDGMENTS

The authors acknowledge financial support from European Union Project No. H2020-MSCA-RISE-2018-823897, "Atlantic." I.B. thanks Cluster of Excellence PhoenixD (EXC 2122, Project No. 390833453) for financial support. Support from the BNSF under Contract No. KP-06-COST/7 is acknowledged (T.A.).

[1] M. Tonouchi, Cutting-edge terahertz technology, Nat. Photonics **1**, 97 (2007).

[2] *Terahertz Optoelectronics*, edited by K. Sakai (Springer, Berlin, 2005).

[3] D. Mittleman, *Sensing with Terahertz Radiation* (Springer, Berlin, 2002).

[4] J. Liu, J. Dai, S. L. Chin, and X. C. Zhang, Broadband terahertz wave remote sensing using coherent manipulation of fluorescence from asymmetrically ionized gases, Nat. Photonics **4**, 627 (2010).

[5] D. J. Cook and R. M. Hochstrasser, Intense terahertz pulses by four-wave rectification in air, Opt. Lett. **25**, 1210 (2000).

[6] M. Kress, T. Loffler, S. Eden, M. Thomson, and H. G. Roskos, Terahertz-pulse generation by photoionization of air with laser pulses composed of both fundamental and second-harmonic waves, Opt. Lett. **29**, 1120 (2004).

[7] T. Bartel, P. Gaal, K. Reimann, M. Woerner, and T. Elsaesser, Generation of single-cycle THz transients with high electric-field amplitudes, Opt. Lett. **30**, 2805 (2005).

[8] X. Xie, J. Dai, and X.-C. Zhang, Coherent Control of THz Wave Generation in Ambient Air, Phys. Rev. Lett. **96**, 075005 (2006).

[9] H. G. Roskos, M. D. Thomson M. Kreß, and T. Löffler, Broadband THz emission from gas plasmas induced by femtosecond optical pulses: From fundamentals to applications, Laser Photonics Rev. **1**, 349 (2007).

[10] I. Babushkin, S. Skupin, A. Husakou, C. Kohler, E. Cabrera-Granado, L. Berge, and J. Herrmann, Tailoring terahertz radiation by controlling tunnel photoionization events in gases, New J. Phys. **13**, 123029 (2011).

[11] S. Herzer, A. Woldegeorgis, J. Polz, A. Reinhard, M. Almassarani, B. Beleites, F. Ronneberger, R. Grosse, G. G. Paulus, U. Hübner, T. May, A. Gopal, An investigation on THz yield from laser-produced solid density plasmas at relativistic laser intensities, New J. Phys. **20**, 063019 (2018).

[12] F. Blanchard, B. E. Schmidt, X. Ropagnol, N. Thiré, T. Ozaki, R. Morandotti, D. G. Cooke, and F. Legare, Terahertz pulse generation from bulk GaAs by a tilted-pulse-front excitation at 1.8 μm, Appl. Phys. Lett. **105**, 241106 (2014).

[13] K. Aoki, J. Savolainen, and M. Havenith, Broadband terahertz pulse generation by optical rectification in GaP crystals, Appl. Phys. Lett. **110**, 201103 (2017).

[14] G. L. Dakovski, B. Kubera, and J. Shan, Localized terahertz generation via optical rectification in ZnTe, J. Opt. Soc. Am. B **22**, 1667 (2005).

[15] S.-C. Zhong, J. Li, Z.-H. Zhai, L.-G. Zhu, J. Li, P. W. Zhou, J. H. Zhao, and Z. R. Li, Generation of 0.19-mJ THz pulses in $LiNbO_3$ driven by 800-nm femtosecond laser, Opt. Express **24**, 14828 (2016).

[16] T. Apostolova and B. Obreshkov, High harmonic generation in crystalline silicon irradiated by an intense ultrashort laser pulse, Eur. Phys. J. D **75**, 267 (2021).

[17] Q. Jin, E. Yiwen, K. Williams, J. Dai, and X.-C. Zhang, Observation of broadband terahertz wave generation from liquid water, Appl. Phys. Lett. **111**, 071103 (2017).

[18] C. Tailliez, X. Davoine, A. Debayle, L. Gremillet, and L. Berge, Terahertz Pulse Generation by Strongly Magnetized, Laser-Created Plasmas, Phys. Rev. Lett. **128**, 174802 (2022).

[19] E. Gaižauskas, V. Vaičaitis, O. Fedotova, and O. Khasanov, Towards broadband terahertz generation due to coherent phonon-polariton excitations in centrosymmetric media, Opt. Mater. Express **5**, 623 (2015).

[20] C. Zhou, Y. P. Liu, Z. Wang, S. J. Ma, M. W. Jia, R. Q. Wu, L. Zhou, W. Zhang, M. K. Liu, Y. Z. Wu, and J. Qi, Broadband Terahertz Generation via the Interface Inverse Rashba-Edelstein Effect, Phys. Rev. Lett. **121**, 086801 (2018).

[21] P. Agarwal, L. Huang, S. Ter Lim, and R. Singh, Electric-field control of nonlinear THz spintronic emitters, Nat. Commun. **13**, 4072 (2022)

[22] D. Ricard, Nonlinear optics in composites and in heterogeneous media, Phys. A (Amsterdam) **157**, 301 (1989).

[23] V. M. Shalaev, *Nonlinear Optics of Random Media* (Springer, Berlin, 2000).

[24] R. Driben, A. Husakou, and J. Herrmann, Supercontinuum generation in aqueous colloids containing silver nanoparticles, Opt. Lett. **34**, 2132 (2009).

[25] J. B. Pendry, Negative Refraction Makes a Perfect Lens, Phys. Rev. Lett. **85**, 3966 (2000).

[26] https://github.com/F1Ulia/SOLPIC/tree/main.

[27] A. Husakou and J. Herrmann, Supercontinuum Generation of Higher-Order Solitons by Fission in Photonic Crystal Fibers, Phys. Rev. Lett. **87**, 203901 (2001).

[28] J. C. Maxwell Garnett, Colours in metal glasses and in metallic films, Philos. Trans. R. Soc. A **203**, 385 (1904).

[29] J. E. Sipe and R. W. Boyd, Nonlinear susceptibility of composite optical materials in the Maxwell Garnett model, Phys. Rev. A **46**, 1614 (1992).

[30] A. Husakou and J. Herrmann, High-power, high-coherence supercontinuum generation in dielectric-coated metallic hollow waveguides, Opt. Express **17**, 12481 (2009).

[31] G. L. Yudin and M. Y. Ivanov, Nonadiabatic tunnel ionization: Looking inside a laser cycle, Phys. Rev. A **64**, 013409 (2001).

[32] T. Apostolova and B. Obreshkov, High harmonic generation from bulk diamond driven by intense femtosecond laser pulse, Diamond Relat. Mater. **82**, 165 (2018).

[33] W. J. Fan, A. P. Abiyasa, S. T. Tan, S. F. Yu, X. W. Sun, J. B. Xia, Y. C. Yeo, M. F. Li, and T. C. Chong, Electronic structures of wurtzite ZnO and ZnO/MgZnO quantum well, J. Cryst. Growth **287**, 28 (2006)

[34] L. S. Meng, Continuous-wave Raman laser in H_2: Semi-classical theory and diode-pumping experiments, Ph.D. thesis, Montana State University, 2002.

[35] K. Kim, A. Taylor, J. Glownia, and G. Rodriguez, Coherent control of terahertz supercontinuum generation in ultrafast laser-gas interactions, Nat. Photonics **2**, 605 (2008).

[36] P. Jürgens, B. Liewehr, B. Kruse, C. Peltz, D. Engel, A. Husakou, T. Witting, M. Ivanov, M. J. J. Vrakking, T. Fennel, and A. Mermillod-Blondin, Origin of strong-field-induced low-order harmonic generation in amorphous quartz, Nat. Phys. **16**, 1035 (2020).

[37] I. Bodurov, I. Vlaeva, A. Viraneva, T. Yovcheva, and S. Sainov, Modified design of a laser refractometer, Nanosci. Nanotechnol. **16**, 31 (2016).

[38] C. Z. Tan, Determination of refractive index of silica glass for infrared wavelengths by IR spectroscopy, J. Non-Cryst. Solids **223**, 158 (1998).

[39] G. Wang, G. K. L. Wong, and J. B. Ketterson, Redetermination of second-order susceptibility of zinc oxide single crystals, Appl. Opt. **40**, 5436 (2001).

[40] M. C. Larciprete, D. Haertle, A. Belardini, M. Bertolotti, F. Sarto, and P. Günter, Characterization of second and third order optical nonlinearities of ZnO sputtered films, Appl. Phys. B **82**, 431 (2006).

[41] V. V. Multian, J. Riporto, M. Urbain, Y. Mugnier, G. Djanta, S. Beauquis, C. Galez, V. Ya Gayvoronsky, and R. Le Dantec, Averaged third-order susceptibility of ZnO nanocrystals from Third Harmonic Generation and Third Harmonic Scattering, Opt. Mater. (Amsterdam) **84**, 579 (2018).

[42] D. Milam, Review and assessment of measured values of the nonlinear refractive-index coefficient of fused silica, Appl. Opt. **37**, 546 (1998).

[43] D. Golde, T. Meier, and S. W. Koch, High harmonics generated in semiconductor nanostructures by the coupled dynamics of optical inter- and intraband excitations, Phys. Rev. B **77**, 075330 (2008).

[44] I. Babushkin, L. Shi, A. Demircan, U. Morgner, J. Herrmann, and A. Husakou, Metallic nanostructures as electronic billiards for nonlinear terahertz photonics, arXiv:2104.14637 [physics.optics].

[45] F. Hache, D. Ricard, and C. Flytzanis, Optical nonlinearities of small metal particles: Surface-mediated resonance and quantum size effects, J. Opt. Soc. Am. B **3**, 1647 (1986).

[46] C. Li, D. Feng, T. Jia, H. Sun, X. Li, S. Xu, X. Wang, and Z. Xu, Ultrafast dynamics in ZnO thin films irradiated by femtosecond lasers, Solid State Commun. **136**, 389 (2005).

[47] W.-M. Wang, Y.-T. Li, Z.-M. Sheng, X. Lu, and J. Zhang, Terahertz radiation by two-color lasers due to the field ionization of gases, Phys. Rev. E **87**, 033108 (2013).

[48] W.-M. Wang, Z.-M. Sheng, Y.-T. Li, Y. Zhang, and J. Zhang, Terahertz emission driven by two-color laser pulses at various frequency ratios, Phys. Rev. A **96**, 023844 (2017).

[49] O. Khasanov, O. Fedotova, G. Rusetsky, and V. Nikiforov, Echo-spectroscopy of nanocomposites, Laser Phys. **29**, 124011 (2019).

[50] O. Fedotova, A. Husakou, G. Rusetsky, O. Khasanov, A. Fedotov, T. Smirnova, U. Sapaev, and I. Babushkin, Mechanisms of terahertz generation under femtosecond pulses propagation in nanocomposites, in *2021 Conference on Lasers and Electro-Optics Europe and European Quantum Electronics Conference*, OSA Technical Digest (Optica, Washington, DC, 2021), p. jsii_1_4.